A Unified Modeling Method of Virtual Synchronous Generator for Multi-Operation-Mode Analyses

Jia Liu[1], Yushi Miura[2], Hassan Bevrani[3] and Toshifumi Ise[4]

1. Osaka University, Japan

2. Nagaoka University of Technology, Japan

3. University of Kurdistan, Iran

4. Nara-Gakuen Incorporated Educational Institution, Japan

IEEE Journal of Emerging and Selected Topics in Power Electronics

DOI: 10.1109/JESTPE.2020.2970025

A Unified Modeling Method of Virtual Synchronous Generator for Multi-Operation-Mode Analyses

Jia Liu, *Member, IEEE*, Yushi Miura, *Member, IEEE*, Hassan Bevrani, *Senior Member, IEEE*, and Toshifumi Ise, *Member, IEEE*

***Abstract*- To provide inertia support for the grid, virtual synchronous generator (VSG) control of inverter-interfaced distributed generators (IIDGs) becomes a focus of worldwide attention. However, a VSG-based IIDG behaves differently in the grid-connected mode, the islanded-single-DG mode, and the islanded-multi-DG mode, whereas the mathematical and physical interpretations of this phenomenon are not well studied. In this paper, we propose a unified modeling method of VSG-based IIDG to analyze its different dynamic performance in each operation mode. The proposed unified formulas can obtain the state-space models of islanded-single-DG mode and islanded-multi-DG mode from that of grid-connected mode for any VSG control method. With the obtained models, for several different types of VSG control in different operation modes, we analyze the distribution and sensitivity of the closed-loop poles and investigate the step responses both analytically and experimentally. These analyses reveal the intrinsic differences and correlations of the dynamics of VSG-based IIDG between each operation mode. These intrinsic features are valid independent from the applied VSG control scheme, thus a test method to evaluate the parameters and performance of an unknown IIDG is derived. The findings of this paper provide important instructions for engineers to model, design and test multi-operation-mode distributed generators.**

***Index Terms*--Distributed power generation, inverters, microgrids, power system dynamics, renewable energy sources, smart grids, state-space methods, synchronverter, virtual synchronous generator.**

LIST OF ABBREVIATIONS

DCL	damping correction loop
DG	distributed generator
DWE	damper windings emulation
GC	grid-connected
IIDG	inverter-interfaced distributed generator
IMDG	islanded-multi-distributed-generator
ISDG	islanded-single-distributed-generator
LPF	low-pass filter
NoD	no dedicated damping
PLL	phase-locked loop
SF	state feedback
SFLPF	state feedback with a low-pass filter
SG	synchronous generator
ROCOF	rate of change of frequency
VSG	virtual synchronous generator

NOMENCLATURE

$\mathbf{0}_{m\times n}$	$m \times n$ zero matrix
$\boldsymbol{A}$	State matrix
$\boldsymbol{B}$	Control input matrix
$\boldsymbol{C}$	Output matrix
D	Virtual damping factor
d	Dimension of vector $\boldsymbol{x}_a$
$\boldsymbol{E}$	Disturbance input matrix
E	Virtual internal electromotive force
$\boldsymbol{F}$	Disturbance output matrix
$\boldsymbol{I}_m$	Identity matrix of size m.
J	Equivalent virtual inertia
J_A	Apparent virtual inertia of method A
K	Synchronizing power coefficient
$K_{p\_pll}^*$	Normalized gain of PI control in PLL
k_p	*ω–P* Droop coefficient
$k_{x\omega}$, k_{xp}, k_{xi}	Feedback gain in SF or SFLPF method
L_{ls}, L_f, L_{line}	Virtual, filter, and line inductance
M^*	Inertia constant (see (67))
n	Number of DGs in IMDG mode
P_0	Active power command
P_d	Damping power
P_{in}	Virtual shaft power
P_{load}	Load active power
P_{out}	Output active power
P_{outf}	Filtered output active power
S_{base}	Rated power
T_f	Time constant of LPF
T_{i_pll}	Time constant of PI control in PLL
$\boldsymbol{u}$, u	Control input vector (or scalar)
V_{base}	Rated voltage
V_{out}, V_{bus}	Inverter output and bus voltage
w	Disturbance input
X	Equivalent output reactance
$\boldsymbol{x}$	State vector
$\boldsymbol{x}_a$	Vector of additional state variables
Δx_{1_pll}, Δx_{2_pll}	State variables of the PLL
$\boldsymbol{y}$	Output vector
Δ	Small-signal perturbation
δ, δ_0	Power angle and its operating point
ζ	Damping ratio
λ	Closed-loop pole (see Table II)
ρ_A	Ratio of J_A/J of the method A
ω_0	Nominal angular frequency and voltage
ω_{bus}	Bus angular frequency
$\widehat{\omega}_g$	Frequency measured by PLL
ω_m	Virtual rotor angular frequency
ω_n	Natural frequency

Superscripts:

$*$	Indicate per unit value
$'$, $''$	(See last paragraph of Section III-B)

Subscripts:

a_i (i = 1, 2)	Parameter a of ith DG in IMDG mode
$a_{(k)}$	kth element of the vector $\boldsymbol{a}$
a_{dcl}	Parameter a of DCL method
$\boldsymbol{a}_g$, a_g	Matrix $\boldsymbol{a}$ (or scalar a) in GC mode model
$\boldsymbol{a}_m$, a_m	Matrix $\boldsymbol{a}$ (or scalar a) in IMDG mode model
$\boldsymbol{a}_s$, a_s	Matrix $\boldsymbol{a}$ (or scalar a) in ISDG mode model
a_{sf}	Parameter a of SF or SFLPF method

I. Introduction

With a successive growth of power generation using renewable energy sources, i.e., photovoltaics and wind turbines, the penetration rate of inverter-interfaced distributed generators (IIDGs) in the power system is in increase at a rapid pace. Unlike conventional centralized generation using synchronous generators (SGs), inverters do not have a rotating mass to provide inertia support for the grid. Therefore, since SGs are gradually replaced by inverters, operators of the power grid are faced with the issue of lack of inertia, which intrinsically leads to a large rate of change of frequency (ROCOF) in the grid. As a result, the power system is prone to frequency fluctuation, and the design of ROCOF-based relays should be reconfigured [1].

To address this issue, the concept of the virtual synchronous generator (VSG) [2]–[4], or virtual synchronous machine [5], or synchronverter [6], [7], has been proposed. It is shown that by adding a short term energy storage to emulate kinetic energy of a rotating mass and mimicking the swing equation of an SG in the control scheme, inverters can also provide inertia support for the grid to restrain its frequency fluctuation, in the same way as an SG [8], [9]. As the principle of these concepts is similar, for convenience sake, all these inverters are referred to as VSG in this paper.

Despite the similar principle, the basic control method of VSG is not unique. For instance, although inertia is emulated similarly in most VSG control strategies, the damping effect can be realized through different approaches. In the literature, VSG control possessing no dedicated damping unit (hereinafter referred to as the NoD method) is adopted in early studies [6], [7], [10], and then improved by dedicated damping methods such as the damper windings emulation (DWE) method [11], [12], the damping correction loop (DCL) method [13], [14], the state feedback (SF) method and its advanced version, the state feedback with a low-pass filter (SFLPF) method [15]. By assigning the closed-loop poles to desired locations, these methods can provide effective damping without affecting the inertial feature of VSG [15]. Besides, other damping methods are also proposed, i.e., using a conventional power system stabilizer [16], increasing output reactance through virtual impedance control [17], adding a high-pass filter term of virtual rotor frequency [18], and using adaptive inertia and/or damping [19]–[21]. Moreover, various inner loop controls can be adopted in a VSG. No inner loop [6], [17], double loops in dq frames [12], [16] or $\alpha\beta$ frames [18], and model predictive control [22] are all reasonable choices.

Owing to its inertia support feature, VSG control is considered as a promising solution of inverter-interfaced distributed generators (IIDG) [17]. Studies on its applications to photovoltaic (PV) systems [23], wind power generation [16] using permanent magnet synchronous generators (PMSG) [24], [25] or doubly-fed induction generators (DFIG) [26] have been reported. Besides, VSG control can be applied to other grid-tied inverters, such as those in energy storage systems [27], [28], in bi-directional battery chargers of electrical vehicles (EVs) providing vehicle-to-grid (V2G) services [18], in voltage source converters (VSC) of high voltage dc transmission (HVDC) system [29]–[33], and in grid-interface dc-ac converters of dc microgrids [34]. Generally, the VSG-based dc-ac converter becomes a standard interface for smart grid integration [35].

One important advantage of VSG control is its ability to make a dispatchable IIDG operation in multi-operation modes, e.g., the grid-connected (GC) mode, the islanded-single-DG (ISDG) mode, and the islanded-multi-DG (IMDG) mode, and to guarantee seamless transfer between these modes without any change in the control scheme. This feature is usually called grid-forming ability, which is inherited from the droop control [8]. Besides, VSG-based IIDG can share the load power autonomously between inverters in the IMDG mode [17].

However, although with the same control, a grid-forming DG behaves differently in each operation mode, and the difference becomes more apparent when the inertial feature is emulated by the VSG control. Unfortunately, the mathematical and physical interpretation of this phenomenon is not well studied in the literature. In most previous works, when a new VSG control method is proposed, its GC mode operation is usually analyzed by means of transfer functions or state-space models, e.g., the NoD method in [10], the DWE method in [11], the DCL method in [13], [14], and the SF/SFLPF methods in [15]. However, the ISDG and IMDG mode operation are not studied in these works. The ISDG mode and IMDG mode of the DWE method is studied through transfer-function models in [8], and state-space model in [17]. However, these models are only valid for DWE method and difficult to be applied for other types of VSG control. In [40], the above damping methods are compared using transfer-function-based analyses for GC mode and ISDG mode operation. With this analytical method, all transfer function should be derived case by case considering the applied control method, the operation mode, and the input and the output. Obviously, the analyses and discussion in [40] is difficult to be extended to new control methods and the IMDG mode operation. Moreover, the motivation of [40] is focused on comparing the pros/cons of different damping methods, whereas the common features of these methods are not studied. Besides, the state-space modeling of an islanded microgrid composed of multiple droop-control-based IIDGs, i.e. the IMDG mode, has well been studied in the literature [36]–[39], and these methods can be easily extended to VSG-based IIDG. However, these works are also only focused on the IMDG mode models, and none of them discussed how to adapt the model to the GC mode. To conclude, as there is no modeling method that can easily cover all major operation modes of a grid-forming DG, it is difficult to find the intrinsic correlations between different operation modes, which are independent of the applied VSG control method.

Consequently, to well interpret the different behaviors of VSG-based IIDG in each operation mode, a unified modeling process to obtain mathematical models of all typical operation modes is expected. Moreover, it should be applicable for any given grid-forming DG; otherwise, the results and conclusions may lose generality. Besides, various VSG control methods are proposed in the literature, whereas a generalized test method to evaluate different types of VSG is not reported yet. The users and the utility may be interested in evaluating the main parameters of an unknown type of VSG by a simple field test.

Motivated by the above issues, we present the following novelties to contribute to the body of knowledge.

1) We propose a unified modeling method to study the active power and frequency control loop, which can be applied to all DGs operating in multi-operation modes, including SGs and IIDGs using existing VSG control methods or droop control technique. This method uses unified formulas to obtain the state-space models of ISDG mode and IMDG mode directly from that of GC mode using the proposed formulas, and this helps us to interpret the differences of each mode mathematically. It is a convenient mathematical tool to model grid-forming DGs for all basic operation modes.
2) With the models obtained through the unified modeling method, we present the closed-loop poles and step responses analyses of various VSG methods in different operation modes, to reveal the intrinsic differences and correlations of the dynamics of VSG-based IIDG for each operation mode. The results illustrate the movement and correlation of dominant poles between different modes and their impact on the dynamic performance. These common features are valid for most investigated VSG controls, and the exceptional conditions are well specified. The revealed analytical solutions of the dominant poles and time constants in each operation mode help us to understand how these dominant poles are determined by the key parameters, and thus this facilitates the parameter design considering multi-operation modes. Especially in the IMDG mode, specific conditions of parameter matching and mismatching between multiple DGs are discussed.
3) We present pole sensitivity analyses to illustrate how the closed-loop poles are affected by intentional or nonintentional variation of some main parameters.
4) We verify the step response analyses by experimental results, which demonstrate the correctness of the proposed unified modeling method and the analyses presented in this paper.
5) Based on the closed-loop poles and step responses analyses, we derive a test method to measure the parameters and evaluate the performance of an unknown IIDG.
6) Previous works in the literature can be verified and better interpreted using the proposed unified modeling method, e.g., the analytical comparison between different VSG control strategies in [40]. The presented unified modeling method is much more efficient to obtain the same analytical results. Based on the given analytical method in [40], all system transfer functions should be derived one by one considering the applied control method, the operation mode, and the input and output..

The following sections are organized as follows. A typical control scheme of VSG-based IIDG and several VSG control methods are introduced in Section II. The proposed unified modeling method and its mathematical and physical interpretation are presented in Section III. In Section IV, closed-loop pole analyses of various VSG methods are discussed to reveal the intrinsic correlations between different operation modes and to study the pole sensitivity. The findings in Section IV are further developed in Section V by step response analyses, and these responses are also verified by the experiment. Based on the observed phenomenon, a test method of an unknown VSG is given in Section VI. Finally, this paper is concluded in Section VII.

II. VSG Control of IIDGs

A. Overall Control Scheme of a VSG-based IIDG

Since this paper is focused on a unified modeling method, a typical control scheme of a VSG-based IIDG proposed in a previous work [15] as shown in Fig. 1 is adopted. It is an RMS-value-based control scheme without using an additional inner voltage or current control loop. Different from VSG control schemes with an inner voltage loop, this type of VSG control regulates the output voltage through the reactive power control loop [6], [17]. Owing to the absence of an inner voltage loop, the active power control loop becomes quite simple and robust, and bus voltage deviation becomes smaller and insensitive to output impedance [17]. Despite the lack of intrinsic current limiter, a previous study [41] shows that the virtual-impedance-based current limiting strategy proposed in [42] is effective for this control scheme. However, this control scheme has no control effect on harmonic components, e.g. the oscillation of LCL filter. Therefore, a dedicated control for harmonic and negative sequences proposed in [43] is applied additionally in the experiment to cover this disadvantage at the cost of increased computational burden in the controller.

In the power generation part, the "governor and virtual inertia" block is the core of VSG control. In the literature, various approaches using different damping technologies are proposed for this part. Since methods capable to assign closed-loop poles facilitate a comparative design and are proved to be effective [15], several closed-loop pole-assignable methods, along with the NoD method, are discussed in this paper, as introduced in the following parts of this section.

In the block "stator impedance adjuster", virtual impedance control is applied. A virtual voltage drop over virtual inductance L_{ls} is generated to adjust the equivalent output reactance X of the inverter as shown in (1).

$$X = \omega_0 \left(L_{ls} + L_f + L_{line} \right) \tag{1}$$

The block "V_{bus} Estimator" estimates the bus voltage from the measurement of output voltage and current, to provide a common reference for the block "Q droop", in which the droop relation between voltage and reactive power is applied [17].

B. Varieties of VSG Control Methods

To emulate the steady-state operation of an SG, its governor model is usually emulated in a dispatchable VSG-based IIDG, as shown in (2).

$$P_{in} = P_0 - k_p(\omega_m - \omega_0) \tag{2}$$

To mimic the dynamics of an SG, swing equation should be emulated. If the effect of damper windings is omitted, the

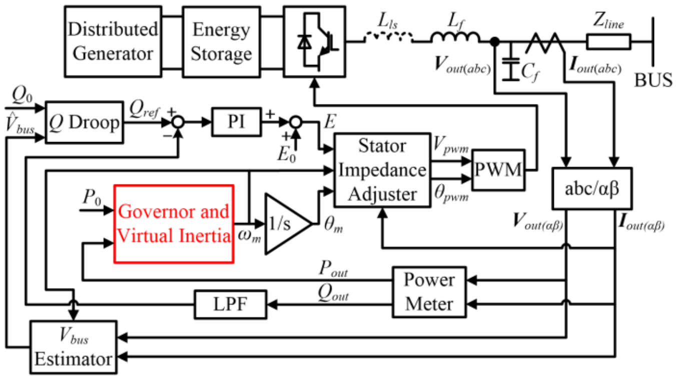

Fig. 1 Typical control scheme of a VSG-based IIDG.

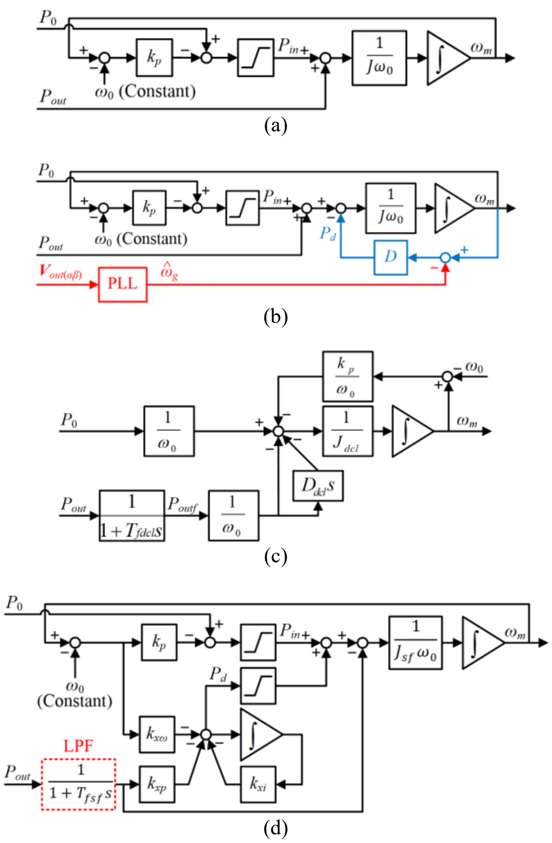

Fig. 2 Existing approaches in the "Governor and Virtual Inertia" block. (a) NoD method; (b) DWE method; (c) DCL method, and (d) SF and SFLPF methods.

swing equation of an SG can be expressed as

$$P_{in} - P_{out} = J\omega_m \frac{\mathrm{d}\omega_m}{\mathrm{d}t} \tag{3}$$

Combining (2) and (3) yields

$$P_0 - P_{out} = J\omega_0 \frac{\mathrm{d}\omega_m}{\mathrm{d}t} + k_p(\omega_m - \omega_0). \tag{4}$$

VSG control emulating (4) in the "governor and virtual inertia" block shown in Fig. 2(a) is referred to as the NoD method. In fact, conventional droop control with a first-order low-pass filter (LPF) is also equivalent to the NoD method [8]. In the NoD method, the damping effect is provided by the droop coefficient k_p . However, k_p should be designed regarding the steady-state operating point, usually based on frequency tolerance and power rating. Therefore, tuning of k_p for the desired damping effect is not available.

A straightforward approach to generate a dedicated damping term is to add the effect of damper windings into (4), as shown in (5), which is referred to as the DWE method.

$$P_0 - P_{out} = J\omega_0 \frac{\mathrm{d}\omega_m}{\mathrm{d}t} + k_p(\omega_m - \omega_0) + D(\omega_m - \omega_{bus}) \tag{5}$$

However, ω_{bus} is difficult to measure directly, thus it is approximated by $\hat{\omega}_g$, which is the angular frequency measured by a phase-locked loop (PLL) from output voltage $\boldsymbol{V}_{out}$ [11], as shown in Fig. 2(b). In [12], an improved version of this method is proposed, in which phase compensation is applied to alleviate the influence of the PLL. As comparisons of state-of-the-art damping methods is not the topic of this paper, only the DWE method in [11] is studied in this paper.

In [13], [14], the DCL method, in which a differential term of P_{out} is used to damp the VSG control as shown in (6)–(7) and Fig. 2(c), is proposed.

$$\omega_m = \frac{1}{k_p + J_{dcl}\omega_0 s}\left(P_0 + k_p\omega_0 - (1 + D_{dcl}s)P_{outf}\right) \tag{6}$$

$$P_{outf} = \frac{1}{1 + T_{fdcl}s} P_{out} \tag{7}$$

It is noteworthy that an LPF shown in (7) is used to attenuate ripples in measured output active power P_{out}. If this LPF is omitted, this method becomes equivalent to the inertial droop control proposed in [8] as discussed in [15].

The SF method proposed in [15] uses a state feedback term to produce damping power, as shown in (8)–(9) and Fig. 2(d).

$$\omega_m = \omega_0 + \frac{1}{J_{sf}\omega_0 s}[P_0 + P_d - k_p(\omega_m - \omega_0) - P_{out}] \tag{8}$$

$$P_d = -k_{x\omega}(\omega_m - \omega_0) - k_{xp}P_{out} - \frac{k_{xi}}{s}P_d \tag{9}$$

It can be further developed by applying an LPF to P_{out} as shown in (10) and Fig. 2(d), and replacing P_{out} by P_{outf} in (8)–(9). This new control method is referred to as the SFLPF method [15].

$$P_{outf} = \frac{1}{1 + T_{fsf}s} P_{out} \tag{10}$$

III. Proposed Unified Modeling Method

In this section, the proposed unified modeling method is presented to study the active power and frequency control loop of a grid-forming DG. This method can directly derive the state-space models of ISDG and IMDG modes from that of GC mode, and it can be applied to SGs and IIDGs with existing VSG control or droop control. Hence, the proposed formulas can help us to understand general differences and intrinsic correlations between various operation modes.

A. GC Mode Model

We recommend to establish the unified modeling method from the GC mode model, as its state-space model is relatively simpler. Moreover, as discussed in Section IV, oscillatory poles appear in the GC mode whereas disappear in the ISDG mode, thus damping effect should be designed based on the GC mode model.

It is well known in the literature that a DG in the GC mode

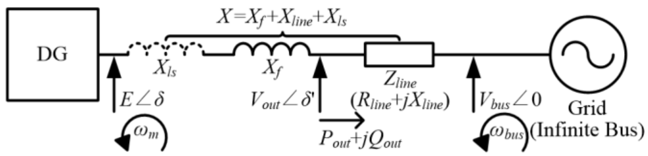

Fig. 3 GC mode model (single DG infinite bus model).

can be considered as a single DG infinite bus system shown in Fig. 3, if the grid is stiff enough. For the case of connected DG to a weak grid, the IMDG model in Part C of this section provides more accurate result. In the single DG infinite bus model, as the bus voltage is dependent on the grid voltage, ω_{bus} should be considered as a disturbance generated by the grid.

It is well-known that the synchronizing power coefficient K of the DG can be expressed as

$$K = \frac{\partial P_{out}}{\partial \delta} \approx \frac{EV_{bus}\cos\delta_0}{X} \approx \frac{V_{base}^2\sqrt{1 - X^{*2}}}{X}, \tag{11}$$

where

$$X^* = XS_{base}/V_{base}^2. \tag{12}$$

The derivative of power angle δ can be represented as

$$\frac{\mathrm{d}\delta}{\mathrm{d}t} = \omega_m - \omega_{bus}. \tag{13}$$

Thus, for each VSG method, the GC mode small-signal state-space model as shown in (14) can be derived from (11), (13) and respective equations in the "governor and virtual inertia" block.

$$\begin{cases} \dot{\boldsymbol{x}}_g = \boldsymbol{A}_g\boldsymbol{x}_g + \boldsymbol{B}_g u_g + \boldsymbol{E}_g w_g \\ \boldsymbol{y}_g = \boldsymbol{C}_g\boldsymbol{x}_g \end{cases} \tag{14}$$

where

$$u_g = \Delta P_0 \tag{15}$$

$$w_g = \Delta\omega_{bus} \tag{16}$$

$$\boldsymbol{y}_g = [\Delta\omega_m \quad \Delta P_{out}]^{\mathrm{T}} \tag{17}$$

$$\boldsymbol{x}_g = [\Delta\omega_m \quad \Delta P_{out} \quad \boldsymbol{x}_a^{\mathrm{T}}]^{\mathrm{T}} \tag{18}$$

where the d (d = 0, 1, 2…) dimension vector $\boldsymbol{x}_a$ is the vector of additional state variables besides $\Delta\omega_m$ and ΔP_{out}. The $\boldsymbol{x}_a$ comes from additional terms such as an LPF or an integrator, thus it is not related to the basic VSG control. It can also include state variables of the turbine model of an SG or inner control loops of a multi-loop VSG. In several basic VSG controls, $\boldsymbol{x}_a$ may not exist (d = 0).

The $\boldsymbol{x}_g$, $\boldsymbol{A}_g$, $\boldsymbol{B}_g$, $\boldsymbol{E}_g$ and $\boldsymbol{C}_g$ depend on the control in the "governor and virtual inertia" block. For instance, for the NoD method,

$$\boldsymbol{x}_g = [\Delta\omega_m \quad \Delta P_{out}]^{\mathrm{T}} \tag{19}$$

$$\boldsymbol{A}_g = \begin{bmatrix} -\frac{k_p}{J\omega_0} & -\frac{1}{J\omega_0} \\ K & 0 \end{bmatrix} \tag{20}$$

$$\boldsymbol{B}_g = \begin{bmatrix} \frac{1}{J\omega_0} & 0 \end{bmatrix}^{\mathrm{T}} \tag{21}$$

$$\boldsymbol{E}_g = [0 \quad -K]^{\mathrm{T}} \tag{22}$$

$$\boldsymbol{C}_g = \boldsymbol{I}_2, \tag{23}$$

From (5), ignoring the PLL dynamics, the GC mode model of the ideal DWE method can be derived as

$$\boldsymbol{A}_g = \begin{bmatrix} -\frac{k_p + D}{J\omega_0} & -\frac{1}{J\omega_0} \\ K & 0 \end{bmatrix} \tag{24}$$

$$\boldsymbol{E}_g = \begin{bmatrix} \frac{D}{J\omega_0} & -K \end{bmatrix}^{\mathrm{T}}, \tag{25}$$

where $\boldsymbol{x_g}$, $\boldsymbol{B_g}$ and $\boldsymbol{C_g}$ are the same as those of the NoD method.

However, in practice, the fast dynamic response of the PLL requires a large loop gain, which makes $\widehat{\omega}_g$ sensitive to the ripples in $\boldsymbol{V}_{out}$. Therefore, the PLL in DWE method is usually tuned to have a moderate response, thus it cannot be neglected. If a typical PLL using dq transformation and a PI controller is applied, the GC mode model of the DWE method becomes

$$\boldsymbol{x}_g = [\Delta\omega_m \quad \Delta P_{out} \quad \Delta x_{1\_pll} \quad \Delta x_{2\_pll}]^{\mathrm{T}} \tag{26}$$

$$\boldsymbol{A}_g = \begin{bmatrix} -\frac{k_p}{J\omega_0} & -\frac{1}{J\omega_0} & \frac{DK_{p\_pll}^*}{J} & \frac{D}{J\omega_0 T_{i\_pll}} \\ K & 0 & 0 & 0 \\ 0 & 0 & -\omega_0 K_{p\_pll}^* & -\frac{1}{T_{i\_pll}} \\ 0 & 0 & \omega_0 K_{p\_pll}^* & 0 \end{bmatrix} \tag{27}$$

$$\boldsymbol{B}_g = \begin{bmatrix} \frac{1}{J\omega_0} & 0 & 0 & 0 \end{bmatrix}^{\mathrm{T}} \tag{28}$$

$$\boldsymbol{E}_g = [0 \quad -K \quad 1 \quad 0]^{\mathrm{T}} \tag{29}$$

$$\boldsymbol{C}_g = [\boldsymbol{I}_2 \quad \boldsymbol{0}_{2\times 2}], \tag{30}$$

This PLL model is not considered in previous studies [11], [15]. Hereinafter, the DWE method ignoring the PLL is referred to as the ideal DWE method, and the one including the PLL is referred to as the DWE method.

Similarly, the GC mode model of the DCL method can be obtained as

$$\boldsymbol{x}_g = [\Delta\omega_m \quad \Delta P_{out} \quad \Delta P_{outf}]^{\mathrm{T}} \tag{31}$$

$$\boldsymbol{A}_g = \begin{bmatrix} -\frac{k_p}{J_{dcl}\omega_0} & 0 & -\frac{1}{J_{dcl}\omega_0} \\ K & 0 & 0 \\ \frac{D_{dcl}K}{T_{fdcl}} & \frac{1}{T_{fdcl}} & -\frac{1}{T_{fdcl}} \end{bmatrix} \tag{32}$$

$$\boldsymbol{B}_g = \begin{bmatrix} \frac{1}{J_{dcl}\omega_0} & 0 & 0 \end{bmatrix}^{\mathrm{T}} \tag{33}$$

$$\boldsymbol{E}_g = \begin{bmatrix} 0 & -K & -\frac{D_{dcl}K}{T_{fdcl}} \end{bmatrix}^{\mathrm{T}} \tag{34}$$

$$\boldsymbol{C}_g = [\boldsymbol{I}_2 \quad \boldsymbol{0}_{2\times 1}]. \tag{35}$$

As the GC mode model of the SF and SFLPF methods are already presented in [15], they are omitted in this paper.

B. ISDG Mode Model

It is straightforward that a DG operating in the ISDG mode can be considered as a single DG single load system as shown

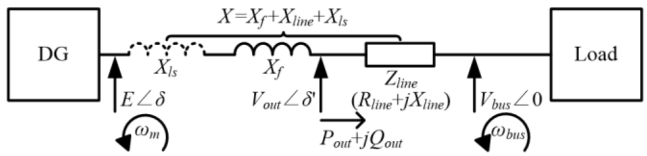

Fig. 4 ISDG mode model (single DG single load model).

in Fig. 4. It is noteworthy that this model can also be extended to multiple loads connected to different buses, as discussed in Part C of this section. In the single DG single load model, as there is no external voltage source, $\Delta\omega_{bus}$ is no longer independent. Therefore, $\Delta\omega_{bus}$ should be eliminated from the disturbance input. Equations (11) and (13) yield

$$w_g = \Delta\omega_{bus} = \Delta\omega_m - \frac{1}{K}\frac{\mathrm{d}\Delta P_{out}}{\mathrm{d}t}, \tag{36}$$

which can be used to eliminate $\Delta\omega_{bus}$. However, it should be noticed that for all DGs, the row relative to ΔP_{out} in GC mode state-space equations is also obtained from (36). Therefore, this row should also be eliminated to avoid redundant equations. Moreover, in the ISDG mode, as the load power $\Delta P_{load} = \Delta P_{out}$ is independent, it should be considered as the disturbance w_s. Therefore, the column related to ΔP_{out} in $\boldsymbol{A}_g$ becomes associated to

$$w_s = \Delta P_{load} \tag{37}$$

in the ISDG mode model.

Consequently, the unified formula to derive the ISDG mode model from any giving GC mode model is

$$\begin{cases} \dot{\boldsymbol{x}_s} = \boldsymbol{A}_s\boldsymbol{x}_s + \boldsymbol{B}_s u_s + \boldsymbol{E}_s w_s \\ y_s = \boldsymbol{C}_s\boldsymbol{x}_s + F_s w_s \end{cases}, \tag{38}$$

where

$$u_s = \Delta P_0 \tag{39}$$

$$y_s = \Delta\omega_m \tag{40}$$

$$\boldsymbol{x}_s = \boldsymbol{x}' + \frac{1}{K}\boldsymbol{E}'\Delta P_{load} \tag{41}$$

$$\boldsymbol{A}_s = \boldsymbol{A}' + [\boldsymbol{E}' \quad \boldsymbol{0}_{(d+1)\times d}]^{\mathrm{T}} \tag{42}$$

$$\boldsymbol{B}_s = \boldsymbol{B}' \tag{43}$$

$$\boldsymbol{E}_s = \boldsymbol{A}'' - \frac{1}{K}\boldsymbol{A}_s\boldsymbol{E}' \tag{44}$$

$$\boldsymbol{C}_s = [1 \quad \boldsymbol{0}_{1\times d}] \tag{45}$$

$$F_s = -\frac{E'_{(1)}}{K} \tag{46}$$

where $\boldsymbol{x}'$, $\boldsymbol{B}'$ and $\boldsymbol{E}'$ are obtained by eliminating the row related to ΔP_{out} from $\boldsymbol{x}_g$, $\boldsymbol{B}_g$ and $\boldsymbol{E}_g$, respectively; $\boldsymbol{A}'$ is obtained by eliminating both the row and column related to ΔP_{out} from $\boldsymbol{A}_g$; $\boldsymbol{A}''$ is obtained by eliminating the row related to ΔP_{out} from the column vector of $\boldsymbol{A}_g$ related to ΔP_{out}.

C. IMDG Mode Model

In this paper, the simplest case of the IMDG mode is considered, which is a two DGs single load system as shown in Fig. 5. Modeling of this model is quite important as it can help us to understand how multi DGs interact in an islanded microgrid. Moreover, if DG1 is modeled as a conventional power plant, this model becomes a weak-grid-connected model of DG2. Furthermore, if DG2 is considered as a cluster of IIDGs, this model can also be used to analyze a simplified high-IIDG-penetration power system.

It is noteworthy that in the field applications, it is likely that the loads are connected to different load buses, as shown in Fig. 5(b). In this case, the values of equivalent output reactance X_1 and X_2 should be adjusted according to the concerned load bus, as it is shown in the figure. That is to say, for the loading transition disturbance at different load buses, we will have different numerical model due to different values of X_1 and X_2. Nevertheless, the difference can be mitigated by applying comparatively large virtual reactance X_{ls1} and X_{ls2}. Similarly, the ISDG mode model can also be extended to the case of multi load buses.

Like the ISDG mode model, $\Delta\omega_{bus}$ should be eliminated from the disturbance input. In the IMDG mode, equation (36) becomes

$$\Delta\omega_{bus} = \Delta\omega_{m1} - \frac{1}{K_1}\cdot\frac{\mathrm{d}\Delta P_{out1}}{\mathrm{d}t} = \Delta\omega_{m2} - \frac{1}{K_2}\cdot\frac{\mathrm{d}\Delta P_{out2}}{\mathrm{d}t} \tag{47}$$

It should be noticed that in the IMDG mode,

$$\Delta P_{load} = \Delta P_{out1} + \Delta P_{out2}. \tag{48}$$

Equations (47)–(48) yield

$$\begin{aligned} w_g = \Delta\omega_{bus} = &-\frac{1}{K_1+K_2}\cdot\frac{\mathrm{d}\Delta P_{load}}{\mathrm{d}t} \\ &+\frac{K_1}{K_1+K_2}\Delta\omega_{m1} + \frac{K_2}{K_1+K_2}\Delta\omega_{m2}. \end{aligned} \tag{49}$$

Therefore, the IMDG mode model can be obtained by eliminating $\Delta\omega_{bus}$ in the GC mode model of both DGs and adding (47) as an extra state equation, as shown in (50).

$$\begin{cases} \dot{\boldsymbol{x}_m} = \boldsymbol{A}_m\boldsymbol{x}_m + \boldsymbol{B}_m\boldsymbol{u}_m + \boldsymbol{E}_m w_m \\ \boldsymbol{y}_m = \boldsymbol{C}_m\boldsymbol{x}_m + \boldsymbol{F}_m w_m \end{cases} \tag{50}$$

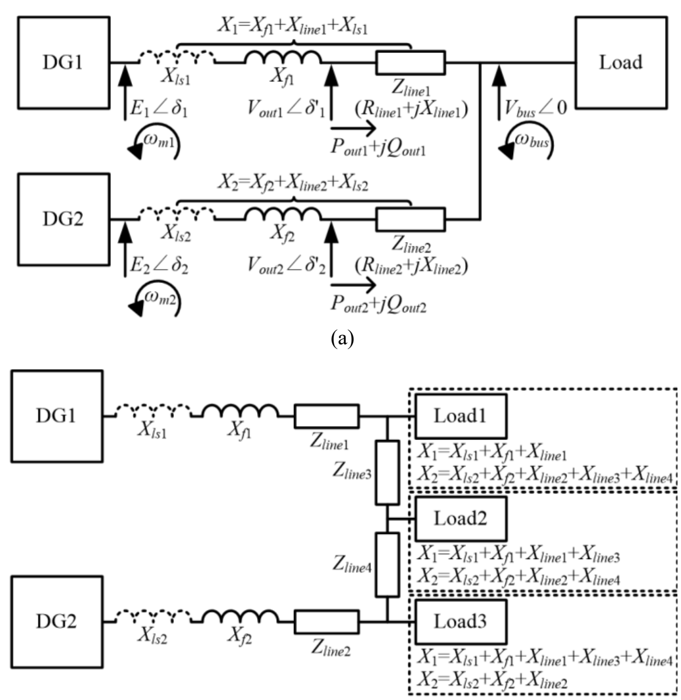

(b)
Fig. 5 (a) IMDG mode model (two DGs single load model) and (b) its extension considering multi load buses.

where

$$\boldsymbol{u}_m = [\Delta P_{0\,1} \quad \Delta P_{0\,2}]^{\mathrm{T}} \tag{51}$$

$$w_m = \Delta P_{load} \tag{52}$$

$$\boldsymbol{y}_m = [\Delta\omega_{m1} \quad \Delta\omega_{m2} \quad \Delta P_{out1} \quad \Delta P_{out2}]^{\mathrm{T}} \tag{53}$$

$$\boldsymbol{x}_m = \begin{bmatrix} \boldsymbol{x}_1' + \dfrac{1}{K_1+K_2}\boldsymbol{E}_1'\Delta P_{load} \\ \boldsymbol{x}_2' + \dfrac{1}{K_1+K_2}\boldsymbol{E}_2'\Delta P_{load} \\ \dfrac{K_2}{K_1+K_2}\Delta P_{out1} - \dfrac{K_1}{K_1+K_2}\Delta P_{out2} \end{bmatrix} \tag{54}$$

$$\boldsymbol{A}_m = \begin{bmatrix} \boldsymbol{A}_{m11} & \boldsymbol{A}_{m12} & \boldsymbol{A}_1'' \\ \boldsymbol{A}_{m21} & \boldsymbol{A}_{m22} & -\boldsymbol{A}_2'' \\ \boldsymbol{A}_{m31} & \boldsymbol{A}_{m32} & 0 \end{bmatrix} \tag{55}$$

$$\boldsymbol{B}_m = \begin{bmatrix} \boldsymbol{B}_1' & \boldsymbol{0}_{(d+1)\times 1} \\ \boldsymbol{0}_{(d+1)\times 1} & \boldsymbol{B}_2' \\ 0 & 0 \end{bmatrix} \tag{56}$$

$$\boldsymbol{E}_m = \begin{bmatrix} \dfrac{1}{K_1+K_2}(K_1\boldsymbol{A}_1'' - \boldsymbol{A}_{m11}\boldsymbol{E}_1' - \boldsymbol{A}_{m12}\boldsymbol{E}_2') \\ \dfrac{1}{K_1+K_2}(K_2\boldsymbol{A}_2'' - \boldsymbol{A}_{m21}\boldsymbol{E}_1' - \boldsymbol{A}_{m22}\boldsymbol{E}_2') \\ -\dfrac{1}{K_1+K_2}(\boldsymbol{A}_{m31}\boldsymbol{E}_1' + \boldsymbol{A}_{m32}\boldsymbol{E}_2') \end{bmatrix} \tag{57}$$

$$\boldsymbol{C}_m = \begin{bmatrix} [1 \quad \boldsymbol{0}_{1\times d}] & \boldsymbol{0}_{1\times(d+1)} & 0 \\ \boldsymbol{0}_{1\times(d+1)} & [1 \quad \boldsymbol{0}_{1\times d}] & 0 \\ \boldsymbol{0}_{1\times(d+1)} & \boldsymbol{0}_{1\times(d+1)} & 1 \\ \boldsymbol{0}_{1\times(d+1)} & \boldsymbol{0}_{1\times(d+1)} & -1 \end{bmatrix} \tag{58}$$

$$\boldsymbol{F}_m = \begin{bmatrix} -\dfrac{1}{K_1+K_2}E_{1(1)}' \\ -\dfrac{1}{K_1+K_2}E_{2(1)}' \\ \dfrac{K_1}{K_1+K_2} \\ \dfrac{K_2}{K_1+K_2} \end{bmatrix} \tag{59}$$

where

$$\boldsymbol{A}_{m11} = \boldsymbol{A}_1' + \left[\frac{K_1}{K_1+K_2}\boldsymbol{E}_1' \quad \boldsymbol{0}_{(d+1)\times d}\right] \tag{60}$$

$$\boldsymbol{A}_{m12} = \left[\frac{K_2}{K_1+K_2}\boldsymbol{E}_1' \quad \boldsymbol{0}_{(d+1)\times d}\right] \tag{61}$$

$$\boldsymbol{A}_{m21} = \left[\frac{K_1}{K_1+K_2}\boldsymbol{E}_2' \quad \boldsymbol{0}_{(d+1)\times d}\right] \tag{62}$$

$$\boldsymbol{A}_{m22} = \boldsymbol{A}_2' + \left[\frac{K_2}{K_1+K_2}\boldsymbol{E}_2' \quad \boldsymbol{0}_{(d+1)\times d}\right] \tag{63}$$

$$\boldsymbol{A}_{m31} = \left[\frac{K_1K_2}{K_1+K_2} \quad \boldsymbol{0}_{1\times d}\right] \tag{64}$$

$$\boldsymbol{A}_{m32} = \left[-\frac{K_1K_2}{K_1+K_2} \quad \boldsymbol{0}_{1\times d}\right] \tag{65}$$

D. Remarks

The proposed formulas can be easily realized in commercial mathematical computing software such as MATLAB so that the ISDG and IMDG mode models can be generated automatically with a given GC mode model. This significantly facilitates the modeling and design of multi-operation-mode DGs.

To better interpret the reason why each mode has a different model, the realized block diagrams of the state-space models of all modes are illustrated in Fig. 6. The most important difference is in existence of an infinite bus in the GC mode, whose frequency is independent of the state variables, thus $\Delta\omega_{bus}$ should be considered as a disturbance. Contrarily, in the islanded modes, bus frequency becomes state-dependent due to the absence of infinite bus, thus $\Delta\omega_{bus}$ should be removed from the disturbances. Meanwhile, as there is no external power generation, load power determines the power generation of the system, thus ΔP_{load} becomes a disturbance in these modes.

By comparing the state vector of the described modes shown in Fig. 6, we notice that the state variable related to ΔP_{out} in the GC mode model is disappeared in the ISDG mode model. This reduces the number of state variables from $2+d$ to $1+d$. As shown in (36), the differential equation related to the state ΔP_{out} is used to eliminate $\Delta\omega_{bus}$ from the disturbances. Therefore, the number of independent differential equations is reduced by one, and the new state variables in the ISDG mode model become a linear combination of $\Delta P_{load}(=\Delta P_{out})$ and the state variables in the GC mode model. As for the IMDG mode model, since the reduction of independent differential equations due to the elimination of $\Delta\omega_{bus}$ does not need to be repeated for each DG, the number of state variables in the IMDG mode model is $n(2+d)-1$. Therefore, $n-1$ new

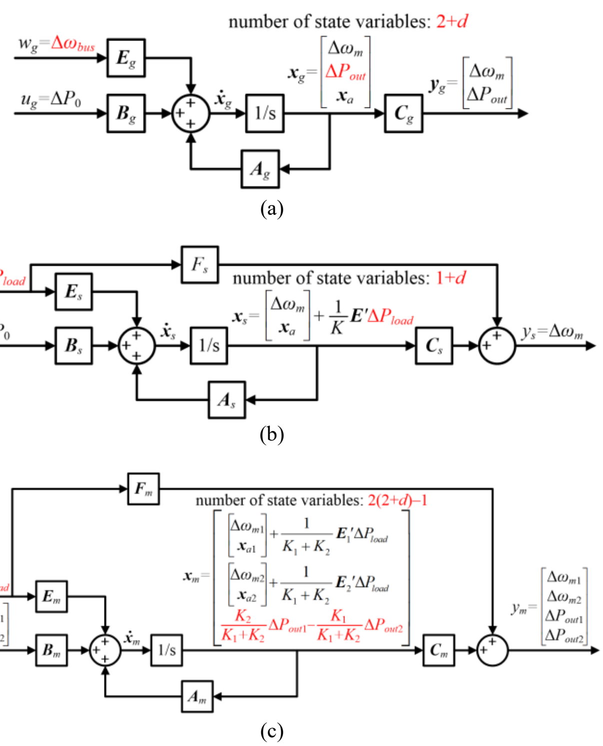

Fig. 6 Block diagrams of (a) the GC mode, (b) the ISDG mode and (c) the IMDG mode state-space models.

state variables are introduced to the IMDG mode model compared to individual n ISDG mode models. Physically, these new $n-1$ state variables are related to the synchronization between the n DGs. For the studied case ($n=2$), one additional state variable appears as shown in Fig. 6(c).

It is noteworthy that the presented models do not include the detailed differential equations of the LCL filter(s), and (11) is a linearized quasi-static approximation for analyzing relatively slow dynamics [44]. Besides, although it is not the case in this paper, some VSG control schemes have inner voltage and current control loops. Including these complete equations will add new state variables in $\boldsymbol{x}_a$; however, the resulted poles are generally much faster than the dominant poles discussed in this paper. The latter are generally far below fundamental frequency owing to the inertial feature of VSG, as shown in the next section. Therefore, for the purpose of this paper, including these equations will only complicate the model and introduce non-dominant poles, whereas the dominant poles will be marginally influenced. Nevertheless, if the proposed modeling method is applied to stability study, it is better to include all these equations during GC mode modeling to make a more complete model. Even in this case, the proposed formulas for deriving ISDG and IMDG mode models can still be applied.

It is also noteworthy that the presented linearized models are approximated models of the real nonlinear systems based on (11), and some specific methods also introduce additional nonlinearities, e.g., the using of PLL in DWE method. These nonlinearities affect the accuracy of the analytical prediction; nevertheless, as it is discussed later in Section V, the resulted errors are generally acceptable.

IV. Closed-Loop Pole Analyses

A. Distribution and Correlation of Poles in Each Mode

In this section, the proposed unified modeling method is used to analyze the distribution of closed-loop poles of each operation mode for different VSG methods, to find the intrinsic correlation between operation modes independent from the control method. The NoD, ideal DWE, DWE, DCL, SF and SFLPF methods are discussed. Their GC mode models are presented in Section III-A, and the ISDG mode and IMDG mode models are derived through the proposed formulas shown in Section III-B and C.

In order to perform a comparative study, the GC mode dominant poles of all methods except the NoD method are assigned to the same locations as shown in (66).

$$\lambda_{g1,2} = \omega_n e^{j(\pi \pm \cos^{-1}\zeta)} = \sqrt{\frac{K}{J\omega_0}}\, e^{j(\pi \pm \cos^{-1} 0.9)} \tag{66}$$

Pole assignment of each method is discussed in [40] thus is not repeated in this paper. The resulted parameters are shown in Table I, which are normalized with individual power ratings to facilitate parameter design of DGs as follows.

$$M^* = J\omega_0^2/S_{base} \tag{67}$$

$$k_p^* = k_p\omega_0/S_{base} \tag{68}$$

$$k_{x\omega}^* = k_{x\omega}\omega_0/S_{base} \tag{69}$$

$$D^* = D\omega_0/S_{base} \tag{70}$$

TABLE I
VSG Parameters

Parameter	Value	Parameter	Value	Parameter	Value
Common Parameters					
V_{base}	200 V	ω_0	377 rad/s	X^*	0.3 pu
S_{base1}	5 kVA	P_0^*	1 pu	M^*	8 s
S_{base2}	2.5 kVA	k_p^*	20 pu	ζ	0.9
Parameters of the DWE Method					
D^*	156 pu	$K_{p\_pll}^*$	0.1 pu	T_{i_pll}	0.5 s
Parameters of the DCL method					
ρ_{dcl}	1.18	D_{dcl}	0.139 s	T_{fdcl}	7.69×10^{-3} s
Parameters of the SF Method					
ρ_{sf}	0.130				
$k_{x\omega}^*$	103 pu	k_{xp}	1.00	k_{xi}	14.3 s^{-1}
Parameters of the SFLPF Method					
ρ_{sflpf}	0.0816	T_{fsf}	6.37×10^{-3} s		
$k_{x\omega}^*$	114 pu	k_{xp}	1.00	k_{xi}	13.9 s^{-1}

TABLE II
Distribution of Closed-Loop Poles in Fig. 7

Method	GC Mode		ISDG Mode	
	VSG-Based	Additional	VSG-Based	Additional
NoD	$\lambda_{g1(\text{NoD})}$, $\lambda_{g2(\text{NoD})}$	null	λ_{s1}	null
Ideal DWE	λ_{g1}, λ_{g2}	null	λ_{s1}	null
DWE	λ_{g1}, λ_{g2}	$\lambda_{g3(\text{DWE})}$, $\lambda_{g4(\text{DWE})}$	$\lambda_{s1\_1(\text{DWE})}$, $\lambda_{s1\_2(\text{DWE})}$	$\lambda_{s2(\text{DWE})}$*
DCL	λ_{g1}, λ_{g2}	λ_{g3}	λ_{s1}	λ_{s2}
SF	λ_{g1}, λ_{g2}	λ_{g3}	λ_{s1}	λ_{s2}
SFLPF	λ_{g1}, λ_{g2}	λ_{g3}, $\lambda_{g4(\text{SFLPF})}$	λ_{s1}	$\lambda_{s2(\text{SFLPF})}$, $\lambda_{s3(\text{SFLPF})}$
Method	IMDG Mode			
	VSG-Based	Counterpart in GC/ISDG	Additional	Counterpart in GC/ISDG
NoD	λ_{m1}, $\lambda_{m2(\text{NoD})}$, $\lambda_{m3(\text{NoD})}$	λ_{s1}, $\lambda_{g1(\text{NoD})}$, $\lambda_{g2(\text{NoD})}$	null	null
Ideal DWE	λ_{m1}, λ_{m2}, λ_{m3}	λ_{s1}, λ_{g1}, λ_{g2}	null	null
DWE	$\lambda_{m1\_1(\text{DWE})}$, $\lambda_{m1\_2(\text{DWE})}$, λ_{m2}, λ_{m3}	$\lambda_{s1\_1(\text{DWE})}$, $\lambda_{s1\_2(\text{DWE})}$, λ_{g1}, λ_{g2}	$\lambda_{m4(\text{DWE})}$, $\lambda_{m5(\text{DWE})}$, $\lambda_{m6(\text{DWE})}$,	$\lambda_{g3(\text{DWE})}$, $\lambda_{g4(\text{DWE})}$, $\lambda_{s2(\text{DWE})}$,
DCL	λ_{m1}, λ_{m2}, λ_{m3}	λ_{s1}, λ_{g1}, λ_{g2}	λ_{m4}, λ_{m5}	λ_{g3}, λ_{s2}
SF	λ_{m1}, λ_{m2}, λ_{m3}	λ_{s1}, λ_{g1}, λ_{g2}	λ_{m4}, λ_{m5}	λ_{g3}, λ_{s2}
SFLPF	λ_{m1}, λ_{m2}, λ_{m3}	λ_{s1}, λ_{g1}, λ_{g2}	λ_{m4}, $\lambda_{m5(\text{SFLPF})}$, $\lambda_{m6(\text{SFLPF})}$, $\lambda_{m7(\text{SFLPF})}$	λ_{g3}, $\lambda_{s2(\text{SFLPF})}$, $\lambda_{s3(\text{SFLPF})}$, $\lambda_{g4(\text{SFLPF})}$

*One of the additional poles becomes conjugate with the VSG-based pole.

$$\rho_A = J_A/J \tag{71}$$

The closed-loop poles of the GC mode, the ISDG mode, and the IMDG mode are shown in Figs. 7(a), 7(b), and 7(c), respectively. In Fig. 7(a), it is clear that $\lambda_{g1,2}$ of the dedicated damping methods, which reflect the VSG feature, are placed to the desired location shown in (66), whereas those of the NoD method have small damping ratio. This indicates that dedicated damping methods have much better dynamics than the NoD method. It is noteworthy that the DWE, DCL, SF, and SFLPF

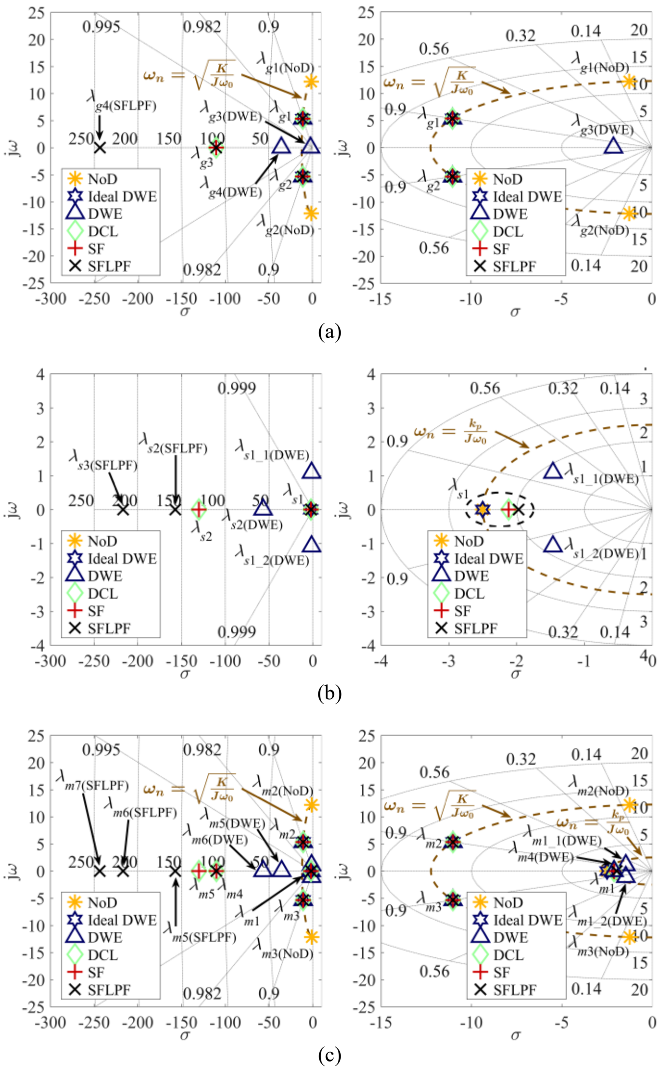

Fig. 7 All closed-loop poles (left side) and zoom-in of dominant poles (right side) of (a) the GC mode, (b) the ISDG mode and (c) the IMDG mode.

methods have additional poles as listed in Table II. The additional poles introduced by $\boldsymbol{x}_a$ in the DCL, SF, and SFLPF methods are non-dominant; however, those in the DWE method, introduced by the PLL, are quite close to the origin, thus they may affect the dynamics of the DWE method.

In [15], it is claimed that assuming K is fixed, as long as ω_n of $\lambda_{g1,2}$ is kept the same, the equivalent inertia remains constant as indicated by (66). However, this conclusion is not verified in the ISDG mode or IMDG mode. As it is shown later in Section V, the dominant pole in the ISDG mode λ_{s1} determines the ROCOF and the time constant of frequency transients, thus it is a very important index of inertia support ability. In [8], it is pointed out that λ_{s1} of the NoD method and the ideal DWE method is

$$\lambda_{s1} = -k_p/(J\omega_0) \tag{72}$$

As shown in Fig. 7(b), (72) is verified. However, λ_{s1} of the other methods do not overlap this desired one, implying that the equivalent inertia of these methods in the ISDG mode is not exactly equal to J. This is because in the case that additional state variables exist, these additional state variables also affect the dominant pole when the mode transfer formulas in Section III-B are applied. However, as long as the additional poles in the GC mode are non-dominant poles, their impact is quite slight. Therefore, as shown in Fig. 7(b) and synthesized in Table II, λ_{s1} of the DCL, SF and SFLPF methods are still close to the desired one, and their additional poles in the ISDG mode remains non-dominant. On the contrary, λ_{s1} of the DWE method is significantly influenced and splits into a pair of conjugated poles λ_{s1_1}, λ_{s1_2} with an additional pole, which results in a slower response with overshoot, as shown in the next section. This implies that the presence of the PLL deteriorates the performance of the DWE method in the ISDG mode. To summary, the equivalent inertia design using the GC mode model based on (66) is also valid in the ISDG mode, as long as the non-dominant poles of the GC mode model are negligible.

By comparing Figs. 7(a) and 7(b), especially the dominant poles $\lambda_{g1,2}$ and λ_{s1}, it can be noticed that the dynamics of the GC mode and ISDG mode of a multi-operation-mode DG are quite different. As long as the non-dominant poles of the GC mode model are negligible, no matter which VSG control method is applied, the GC mode model is a second-order system, and the ISDG mode model is a first-order system, and their respective time constants τ_g, τ_s can be quite different as shown in (73)–(74). The reason for this reduced order is discussed previously in Section III-D.

$$\tau_g = \frac{1}{\left|\mathrm{RE}\left(\lambda_{g1,2}\right)\right|} = \frac{1}{\zeta}\sqrt{\frac{J\omega_0}{K}} \tag{73}$$

$$\tau_s = \left|\frac{1}{\lambda_{s1}}\right| = \frac{J\omega_0}{k_p} \tag{74}$$

Generally, small τ_g and large ζ are preferred for fast and non-oscillatory power response in the GC mode, and large τ_s is preferred for slow frequency fluctuation in the ISDG mode. From (73)–(74), as k_p cannot be tuned freely, large J, ζ, and small X are preferable. As shown in Fig. 7(a), large ζ is available through a proper closed-loop assignment. It is noteworthy that X should not be too small, because the output impedance of DG is preferred to be inductive in order to ensure the power decoupling between active and reactive power.

In the IMDG mode pole plot shown in Fig. 7(c), the same normalized parameters in Table I are applied to both DGs. This is referred to as the parameter matching case in this paper. In this case, we found that the IMDG mode poles are a simple assembly of those of GC mode and ISDG mode. As shown in Fig. 7 and concluded in Table II, this important conclusion is valid for both dominant and non-dominant poles of all discussed methods. For example, the dominant poles of any VSG control in the IMDG mode $\lambda_{m1,2,3}$ can be obtained from the GC mode and the ISDG mode as

$$\begin{cases} \lambda_{m1} = \lambda_{s1} \\ \lambda_{m2,3} = \lambda_{g1,2} \end{cases}. \tag{75}$$

This phenomenon can be interpreted as follows. GC mode poles illustrate how the DG is synchronized to another voltage source (an infinite bus), ISDG mode poles imply how the IIDG forms a grid by itself. The IMDG mode is also a self-formed grid as the ISDG mode, and meanwhile, a synchronizing effect between two DGs also exists. Therefore, it is comprehensible that one of the IMDG mode poles shows a self-formed-grid feature and the others illustrate a synchronizing feature.

This new finding implies that the IMDG mode behaviors cover those of GC and ISDG modes, thus both time constants τ_g and τ_s can be observed in the IMDG mode. Therefore, the design and testing of a multi-operation-mode DG can be focused on its IMDG mode. Moreover, (75) implies that existing equivalent inertia and damping design methods based on the GC mode model can be directly applied to the IMDG mode. As it is discussed in the next section, small τ_g is still preferred for fast power response, and large τ_s is still preferred for slow frequency fluctuation. It should be noticed that in the parameter mismatching case, the IMDG mode poles are determined by both DGs and are affected by parameter mismatching, thus they no longer perform as a simple assembly of the GC and ISDG modes poles. However, λ_{m1} and $\lambda_{m2,3}$ are still related to λ_{s1} and $\lambda_{g1,2}$ of each DG, respectively. Although it is difficult to find a generalized correlation like (75), a numerical solution can be easily obtained using the proposed unified modeling method.

B. Sensitivity of the Closed-Loop Poles

In order to investigate how the poles are affected by intentional or nonintentional parameter variation, two sensitivity studies are performed. As shown in (75), λ_{m1} and λ_{m2} describe almost all important dynamics covering all the three operation modes; therefore, the following discussions are focused on these two poles. Parameters are the same as those in Table I, except that S_{base2} is changed to 5 kVA to facilitate the interpretation of the parameter mismatching case.

An intentional variation of of J_1 and J_2 by the manufacturer is considered in Fig. 8. In this case, the variation is applied to DG1 and DG2 equally, and all control methods are redesigned according to (66) to keep ζ of $\lambda_{g1}(= \lambda_{m2})$ constant. Therefore, as shown in Fig. 8, ζ of λ_{m2} is kept unchanged, except that the NoD method shows a decreasing ζ because the absence of dedicated damping. This variation coincides with the expression shown in [15]. Meanwhile, ζ of λ_{m1} also remains unchanged as λ_{m1} is a real pole except that of the DWE method. On the other hand, ω_n of both λ_{m1} and λ_{m2} increases while J_1 and J_2 increase. The observed variation also well coincides with (66) and (72).

In Fig. 9, we consider an unintentional mismatching of X_1 and X_2. According to Fig. 5(b), the IMDG mode model is affected by the variation of the location of loading disturbance. As the manufacturer cannot predict this variation, all the control parameters are kept unchanged. The horizontal axis of Fig. 9 indicates the % mismatching of X_1 and X_2, e.g., 10 % means X_1 is increased by 10 % and X_2 is decreased by 10 %. Fig. 9 shows that both λ_{m1} and λ_{m2} are barely affected by this reactance mismatching, except that ω_n of λ_{m2} slightly decreases while the mismatching increases. This result implies that the location of loading disturbance can be neglected in the pole analyses. However, as studied in [17], the reactance mismatching affects the zeros of the transfer functions from the input ΔP_{load}, thus it still has a considerable impact on the dynamic performance of IMDG mode especially during the period right after a loading transition, as shown later in Section V-C.

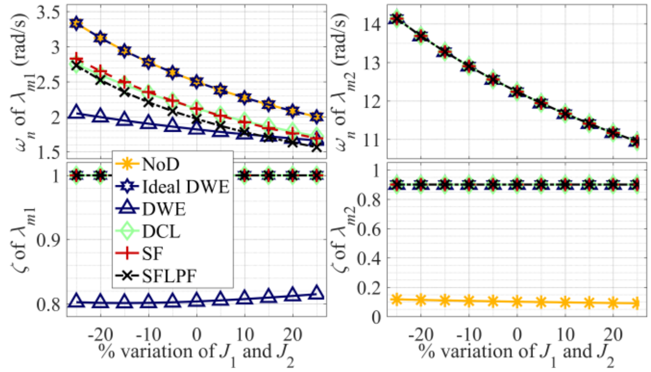

Fig. 8 Sensitivity of dominant poles to variation of J_1 and J_2.

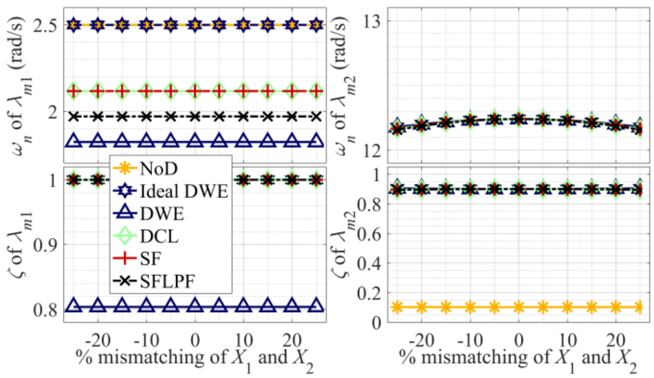

Fig. 9 Sensitivity of dominant poles to mismatching of X_1 and X_2.

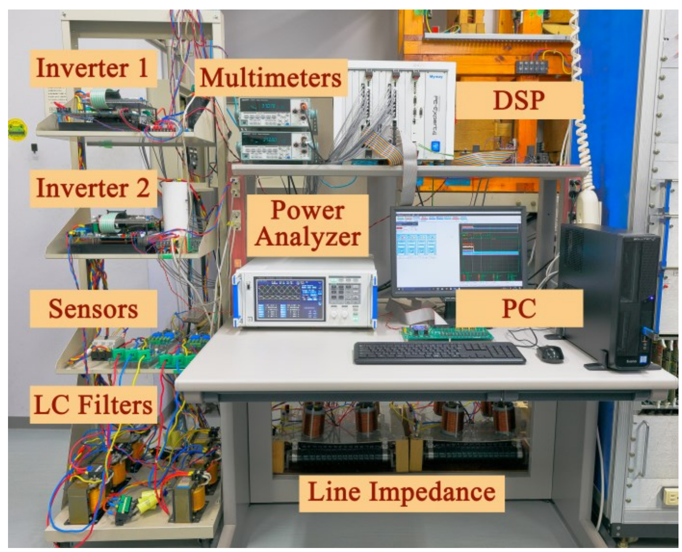

(a)

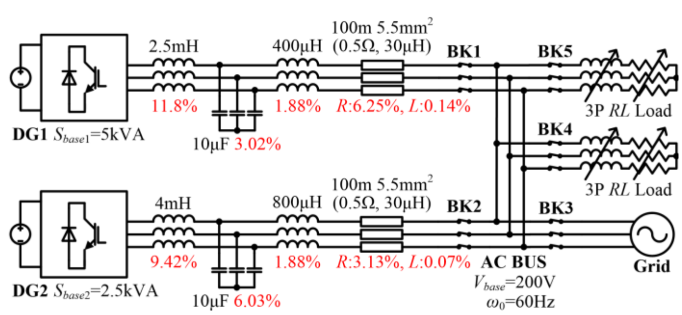

(b)

Fig. 10 Experimental testbed; (a) overview, and (b) circuit diagram.

V. Step Response Analyses and Experimental Verification

From the state-space equations of all operation modes obtained through the proposed unified formulas, $\boldsymbol{G_c}(s)$ and $\boldsymbol{G_d}(s)$ of each operation mode, which are the output transfer function matrix from the control inputs and the disturbance input, respectively, can be calculated as (76)–(77).

$$\boldsymbol{G_c}(s) = \boldsymbol{C}(s\boldsymbol{I} - \boldsymbol{A})^{-1}\boldsymbol{B} \tag{76}$$

$$\boldsymbol{G_d}(s) = \boldsymbol{C}(s\boldsymbol{I} - \boldsymbol{A})^{-1}\boldsymbol{E} + \boldsymbol{F} \tag{77}$$

Thus, it is straightforward to analyze the responses of outputs during a given step change of an input.

Since comparisons of analytical responses and experimental results in the GC mode are already studied in [40], in this paper, we focus on the ISDG and IMDG modes. Several case studies are discussed to understand how the closed-loop poles presented in Section IV affect dynamic response. The results are verified by experiments using the testbed shown in Fig. 10. The control parameters of both DGs are the same as those in Table I, if not otherwise specified. In the following studies, to focus on the behaviors of active power and frequency, the reactive power of the loads is set to about zero. Moreover, to clearly investigate the performance of the primary control, the secondary control to restore the frequency in an islanded microgrid [4] is not considered. Therefore, according to (2), steady state frequency deviation occurs as long as the load power ($= P_{in}$) is not equal to P_0.

A. Loading Transition in the ISDG Mode

In this case, BK1 is closed and both BK2 and BK3 are open, and the load changes from 2.17 kW to 4.87 kW. The analytical responses and experimental results are shown in Fig. 11. It is demonstrated that the analytical responses are verified by the experimental results, except for some differences in the first milliseconds observed in the DWE method. This is because the PLL in the DWE method is also influenced by $\boldsymbol{V_{out}}$ fluctuation caused by the loading transition, which is not considered in (26)–(30). Besides, the frequency of $\boldsymbol{V_{out}}$ does not exactly equal to ω_{bus} during transients. Moreover, as the PLL is nonlinear due to a trigonometric function, it is difficult to exactly predict its response using small-signal linearization. Similar phenomena can be observed in the analytical responses of the DWE method in the following case studies.

As no oscillation mode appears in this case as shown in Fig. 7(b), even the NoD method does not show any oscillation. Thus the responses shown in Fig. 11 are similar to a first-order response, and their time constants are quite close to τ_s shown in (74). This implies that the equivalent inertia of each method indicated by λ_{s1} in Fig. 7(b) is almost the same. The only exception is the DWE method, which shows a second-order response with overshoot. This unexpected performance is caused by the PLL which is well predicted by the analytical response shown in Fig. 11(a) and the given discussion on Fig. 7(b). Besides, it can also be observed that the frequency of dedicated damping methods drops much faster than the NoD method in the first milliseconds. This implies that effective damping and the first stage ROCOF are in a trade-off relation. Nevertheless, this first stage drop does not affect the time constant of frequency fluctuation.

B. Power Command Change in the IMDG Mode

In this case, both BK1 and BK2 are closed and BK3 is open, and a 7.21 kW load is connected to the bus. The initial power command P_0^* of both DGs are 1.0 pu, and that of DG1 is changed to 0.5 pu at 0 s. The analytical responses and experimental results of the parameter matching case are shown in Fig. 12. It is noteworthy that for the responses of P_{out1} and P_{out2} in Fig. 12(a), the DCL method overlaps the DWE and ideal DWE methods, and the SFLPF method overlaps the SF method. Like the previous case, the analytical responses are well verified by the experimental results except for the first stage of the DWE method. Besides, there is a little difference in oscillation frequency and attenuation time constant of the NoD method. This is because accurate linearization of (11) requires recalculation of K based on the operating point of the power angle δ, and the latter is affected by the output active power. In the presented analytical results, for convenience, K is considered to be fixed based on the rated power as shown in (11). Nevertheless, this difference is not significant.

Fig. 12 shows that the responses of DG frequency are similar to that of ISDG mode. This implies that the inertia support ability of VSG is mainly dependent on λ_{m1}. However, the oscillation in the NoD method implies that the responses related to $\lambda_{m2,3}$ are also superposed. On the other hand, $\lambda_{m2,3}$ dominate the responses of DG power to power command change. These conclusions are valid for all discussed methods. It can be noticed that the SF and SFLPF methods are the best solutions among the studied methods, because they have an extra zero to optimize transient response [15]. As detailed comparisons between damping methods are discussed in [40], this topic is not further developed in this paper.

Similar experiments for the parameter mismatching case are also performed. In this study, the parameters of DG2 are kept unchanged, whereas DG1 is redesigned to make M^*= 12 s and

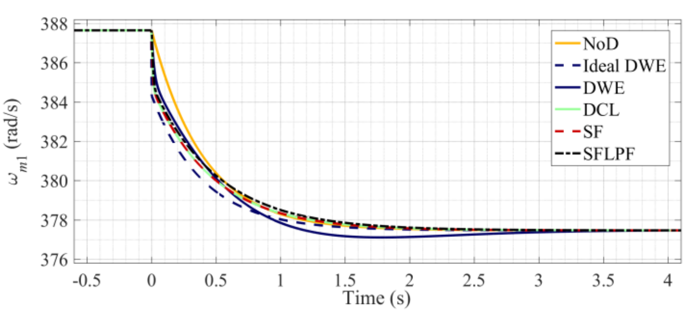

(a)

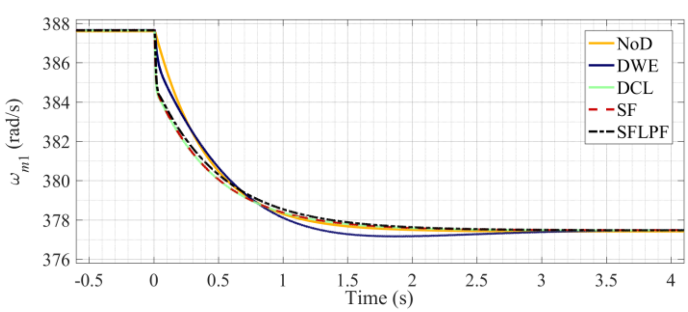

(b)

Fig. 11 Step responses during loading transition in the ISDG mode; (a) analytical results, and (b) experimental results.

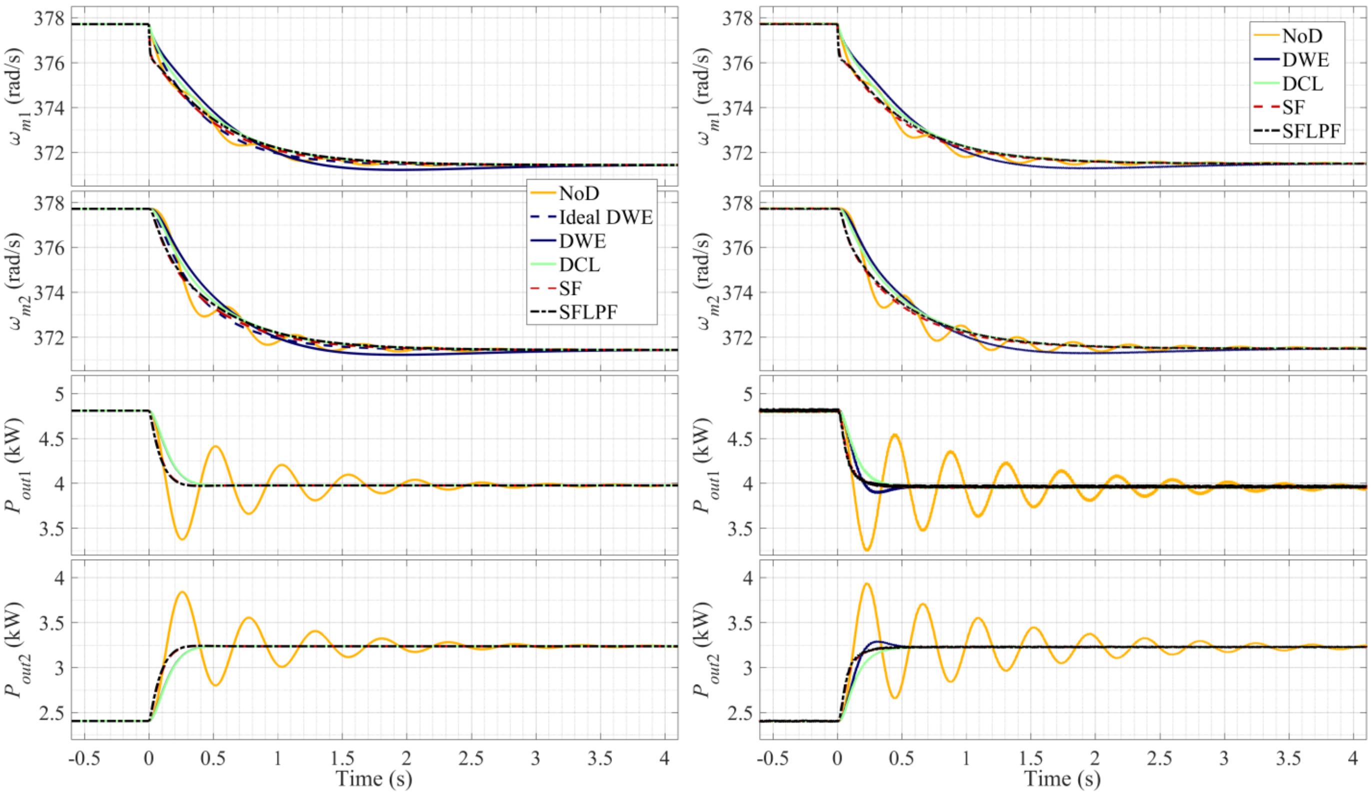

(a) (b)

Fig. 12 Step responses during power command change in the IMDG mode (parameter matching case); (a) analytical results, and (b) experimental results.

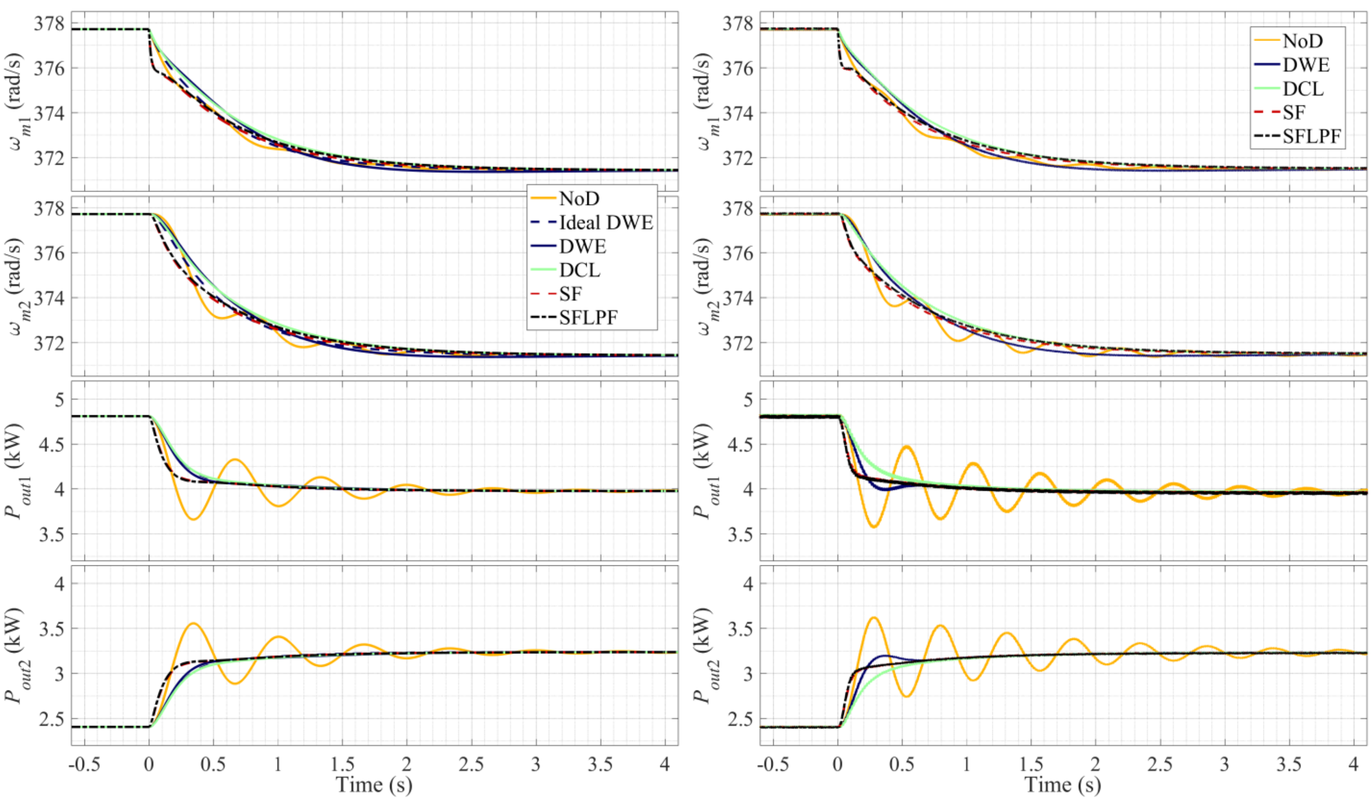

(a) (b)

Fig. 13 Step responses during power command change in the IMDG mode (parameter mismatching case); (a) analytical results, and (b) experimental results.

$X^* = 0.6$ pu, and the resulted parameters are shown in Table III. Again, as shown in Fig. 13, the analytical responses coincide with the experimental results except for the first stage of the DWE method. In this case, for all discussed methods, the impact of λ_{m1} also appears in responses of DG power, whereas it does not appear in Fig. 12. This is because, in the parameter

TABLE III
DG1 PARAMETERS IN THE PARAMETER MISMATCHING CASE

Common Parameters and Parameters of the DWE Method					
Parameter	Value	Parameter	Value	Parameter	Value
X^*	0.6 pu	M^*	12 s	D^*	120 pu
Parameters of the DCL Method					
ρ_{dcl}	1.18	D_{dcl}	0.255 s	T_{fdcl}	1.46×10^{-2} s
Parameters of the SF Method					
ρ_{sf}	0.134	$k_{x\omega}^*$	80.1 pu	k_{xi}	7.83 s^{-1}
Parameters of the SFLPF Method					
ρ_{sflpf}	0.126	$k_{x\omega}^*$	84.5 pu	k_{xi}	7.65 s^{-1}

*Parameters not specified are the same as those in Table I.

matching case, λ_{m1} is canceled by a zero in the transfer functions $\frac{\Delta P_{outj}}{\Delta P_{0i}}$ $(i, j = 1, 2)$, whereas this cancellation does not occur if the parameters are mismatched.

C. Loading Transition in the IMDG Mode

The circuit configuration of this case is the same as that of Part B, and a loading transition from 4.49 kW to 7.18 kW is investigated. As the parameter matching case is already studied in [15], [17], the parameter mismatching case is discussed in this paper as shown in Fig. 14. This figure shows that the analytical results resemble the experimental results, except for slight errors due to the approximation of K and the PLL of DWE method which is discussed previously.

For all discussed methods in this case, similarly to Figs. 12 and 13, the responses of DG frequency shown in Fig. 14 depend mainly on λ_{m1}, whereas the behaviors related to $\lambda_{m2,3}$ are also observed. In the responses of DG power, same as Fig. 13, transients caused by both λ_{m1} and $\lambda_{m2,3}$ can be observed. It can be noticed that the DG with smaller X tends to share more initial power right after the event, whereas afterward, the DG with larger J tends to share more transient power. Besides, unlike Fig. 12, the SF and SFLPF methods do not respond faster than other methods, because the above-mentioned additional zero of these methods only affect the transfer functions from the inputs $\Delta P_{0\,i}$. In the parameter matching case as shown in [15], [17], $\lambda_{m2,3}$ are cancelled by zeros in transfer function $\frac{\Delta\omega_{mi}}{\Delta P_{load}}$, and both λ_{m1} and $\lambda_{m2,3}$ are cancelled by zeros in transfer function $\frac{\Delta P_{outi}}{\Delta P_{load}}$. As a result, for all discussed methods, the responses of DG frequency become exactly the same as the ISDG mode, and the responses of DG power become single steps. Owing to the simple and fast dynamic responses, generally, parameter matching is preferred in field applications.

VI. TEST METHOD OF AN UNKNOWN VSG

Based on the given discussions in Sections VI and V, a test method to identify an unknown VSG can be derived: First, make a loading transition test in the ISDG mode similar to that shown in Section V-A, to measure the droop coefficient k_p and the equivalent moment of inertia J. It is well known that k_p can be measured from the equation

$$k_p = -\frac{P_{out}(\infty) - P_{out}(0^-)}{\omega_m(\infty) - \omega_m(0^-)} \tag{78}$$

where ∞ indicates the steady state and 0^- indicates the initial

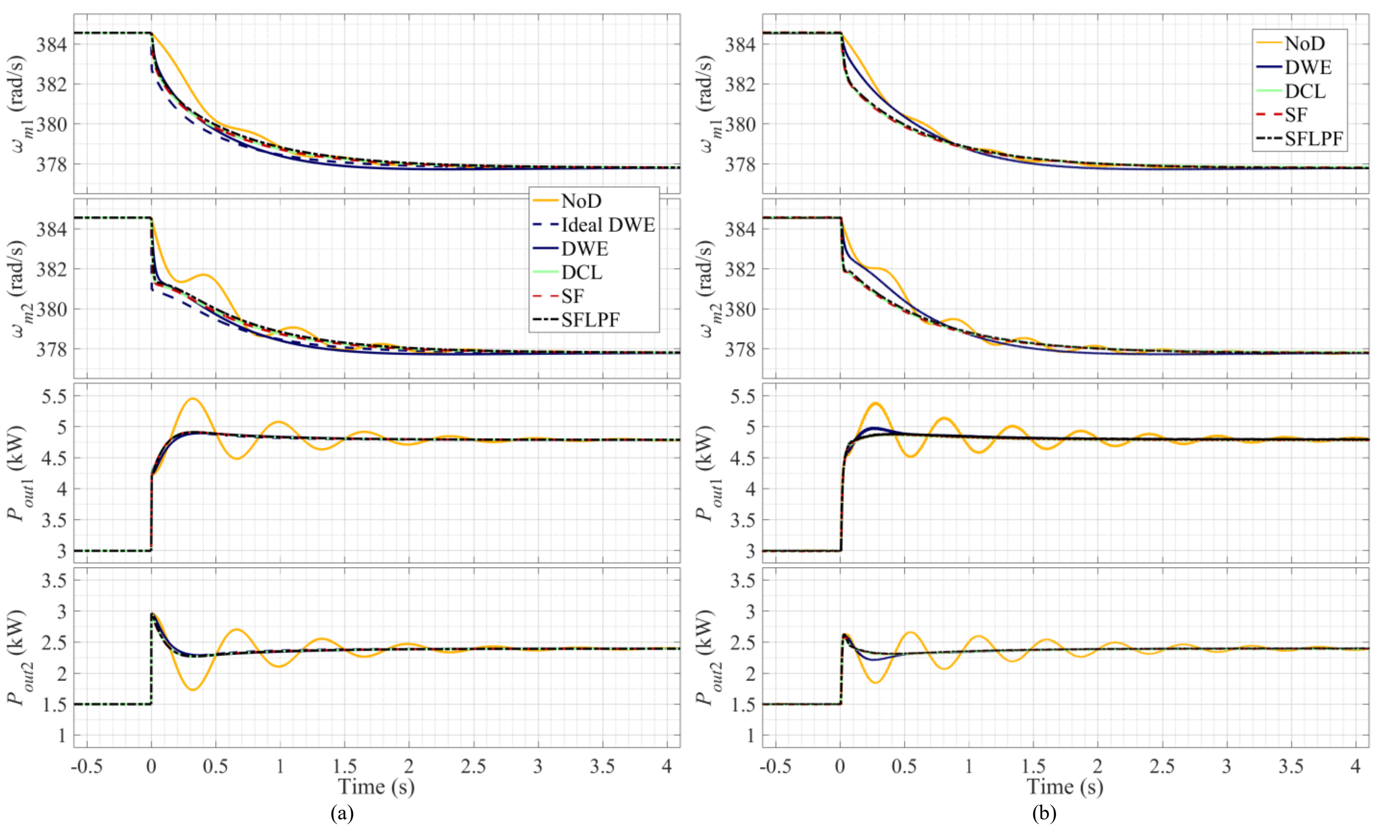

Fig. 14 Step responses during loading transition in the IMDG mode (parameter mismatching case); (a) analytical results, and (b) experimental results.

TABLE IV
MEASURED VALUE OF k_p AND J

Method	k_p		J	
	Value (W·s/rad)	Error (%)	Value (kg·m^2)	Error (%)
Designed	265.26	-	0.2814	-
NoD	265.12	-0.054	0.2899	3.02
DWE	265.29	0.014	0.2809	-0.19
DCL	265.26	0.000	0.2833	0.65
SF	265.30	0.017	0.2826	0.40
SFLPF	265.37	0.042	0.3078	9.36

state. Afterward, by measuring the transient time constant τ_s, J can be calculated through (74). Here, it is better to measure $2\tau_s$ by finding the 86.5% changing point [45], because Fig. 11 shows that the dedicated damping terms accelerate the response before τ_s, and this influence almost disappears at $2\tau_s$. Table IV shows the measured k_p and J using the data of Fig. 11(b). The results demonstrate that 1 ‰ and 10 % precision measurements are achieved for k_p and J, respectively.

Secondly, apply a step change in power command P_0 in the GC mode and record the response of P_{out}. It is well known that the damping ratio ζ of a second-order system can be measured from the maximum percent overshoot, and the time constant τ_g can be measured from the settling time [45], thus the synchronizing coefficient K can be calculated through (73). Furthermore, the output reactance X can be obtained from K through (11). However, it is noteworthy that the accuracy of the above calculation is quite limited, due to the nonlinearity of K and the approximation error in the identification of second-order system. Therefore, in field applications, it is more practical to directly use the maximum percent overshoot and the settling time to evaluate the synchronizing performance.

This method is quite simple and practical in the field applications. As the proposed test method is proved applicable for various types of VSG, it may become a favorite candidate in a future standard.

VII. CONCLUSIONS

In this paper, we propose a unified modeling method to obtain the ISDG mode and IMDG mode state-space models from that of GC mode. This method can be applied to any multi-operation-mode DG, including IIDGs using VSG or droop control and conventional SGs. Therefore, the proposed modeling method provides a universal mathematical tool for designing multi-operation-mode DGs. With the help of the proposed method, we give mathematical and physical interpretations for the different behaviors of grid-forming DGs in different operation modes and perform the closed-loop pole analyses and step response analyses for several existing VSG control methods. These analyses reveal the intrinsic differences and correlations of the dynamics of VSG-based IIDG between each operation mode. The sensitivity of poles is evaluated considering intentional or unintentional parameter variation. Moreover, we verify the step response analyses by experimental results and derive a test method to measure the parameters and evaluate the performance of an unknown VSG. Some important findings presented in these analyses are as follows.

1) The equivalent inertia design using the GC mode model based on (66) is also verified in the ISDG mode and the IMDG mode, as long as the non-dominant poles of the GC mode model are negligible.
2) For an IIDG, the GC mode is basically a second-order system, and its dominant poles mainly determine the response of active power. The ISDG mode is basically a first-order system, and its dominant pole mainly determines the inertia support ability. The GC mode system is preferred to be fast and non-oscillatory, and the ISDG mode system is preferred to be slow.
3) In the parameter matching case of the IMDG mode, poles are the assembly of those of GC and ISDG modes. Moreover, certain dominant poles may be canceled by zeros. e.g., λ_{m1}, which represents ISDG mode dynamics, is always canceled in DG power responses. Therefore, this case is preferable in field applications.
4) The responses of the parameter mismatching case of the IMDG mode cover all dynamic features of IIDGs, as pole cancelation does not occur. Therefore, this case may be an interesting subject for control design and product testing. Transient power sharing in this case depends on the output reactance and inertia of the DGs. On the other hand, the location of dominant poles are not markedly affected by the parameter mismatch.
5) The droop coefficient and moment of inertia can be accurately measured in the ISDG mode, and the oscillation feature can be evaluated in the GC mode.

Our future works are subjected to extending the proposed formulas to the case of $n > 2$ and to the voltage–reactive power control.

REFERENCES

[1] J. Fang, H. Li, Y. Tang, and F. Blaabjerg, "On the inertia of future more-electronics power systems," *IEEE J. Emerg. Sel. Topics Power Electron.*, vol. 7, no. 4, pp. 2130–2146, Dec. 2019.

[2] J. Driesen and K. Visscher, "Virtual synchronous generators," in *Proc. IEEE Power Energy Soc. Gen. Meeting—Convers. Del. Elect. Energy 21st Century*, Pittsburgh, PA, USA, 2008, pp. 1–3.

[3] K. Sakimoto, Y. Miura, and T. Ise, "Stabilization of a power system with a distributed generators by a virtual synchronous generator function," *8th IEEE Int. Conf. Power Electron. (ICPE - ECCE Asia)*, Jeju, Korea, 2011, pp. 1498–1505.

[4] H. Bevrani, B. François, and T. Ise, *Microgrid Dynamics and Control*. Hoboken, NJ, USA: Wiley, 2017, pp. 307–434.

[5] H.-P. Beck and R. Hesse, "Virtual synchronous machine," in *Proc. 9th Int. Conf. Elect. Power Quality Util.*, Barcelona, Spain, 2007, pp. 1–6.

[6] Q.-C. Zhong and G. Weiss, "Synchronverters: inverters that mimic synchronous generators," *IEEE Trans. Ind. Electron.*, vol. 58, no. 4, pp. 1259–1267, April 2011.

[7] Q.-C. Zhong, P.-L. Nguyen, Z. Ma, and W. Sheng, "Self-synchronized synchronverters: inverters without a dedicated synchronization unit," *IEEE Trans. Power Electron.*, vol. 29, no. 2, pp. 617–630, Feb. 2014.

[8] J. Liu, Y. Miura, and T. Ise, "Comparison of dynamic characteristics between virtual synchronous generator and droop control in inverter-based distributed generators," *IEEE Trans. Power Electron.*, vol. 31, no. 5, pp. 3600–3611, May 2016.

[9] Y. Hirase, K. Sugimoto, K. Sakimoto and T. Ise, "Analysis of resonance in microgrids and effects of system frequency stabilization using a virtual synchronous generator," *IEEE J. Emerg. Sel. Topics Power Electron.*, vol. 4, no. 4, pp. 1287–1298, Dec. 2016.

[10] H. Wu, X. Ruan, D. Yang, X. Chen, W. Zhao, Z. Lv, and Q.-C. Zhong, "Small-signal modeling and parameters design for virtual synchronous generators," *IEEE Trans. Ind. Electron.*, vol. 63, no. 7, pp. 4292–4303, July 2016.

[11] T. Shintai, Y. Miura, and T. Ise, "Oscillation damping of a distributed

generator using a virtual synchronous generator," *IEEE Trans. Power Del.*, vol. 29, no. 2, pp. 668–676, April 2014.
[12] L. Huang, H. Xin, and Z. Wang, "Damping low-frequency oscillations through VSC-HVdc stations operated as virtual synchronous machines," *IEEE Trans. Power Electron.*, vol. 34, no. 6, pp. 5803–5818, June 2019.
[13] S. Dong and Y. C. Chen, "Adjusting synchronverter dynamic response speed via damping correction loop," *IEEE Trans. Energy Convers.*, vol. 32, no. 2, pp. 608–619, June 2017.
[14] S. Dong and Y. C. Chen, "A method to directly compute synchronverter parameters for desired dynamic response," *IEEE Trans. Energy Convers.*, vol. 33, no. 2, pp. 814–825, June 2018.
[15] J. Liu, Y. Miura, and T. Ise, "Fixed-parameter damping methods of virtual synchronous generator control using state feedback," *IEEE Access*, vol. 7, pp. 99177–99190, 2019.
[16] Y. Ma, W. Cao, L. Yang, F. Wang, and L. M. Tolbert, "Virtual synchronous generator control of full converter wind turbines with short-term energy storage," *IEEE Trans. Ind. Electron.*, vol. 64, no. 11, pp. 8821–8831, Nov. 2017.
[17] J. Liu, Y. Miura, H. Bevrani, and T. Ise, "Enhanced virtual synchronous generator control for parallel inverters in microgrids," *IEEE Trans. Smart Grid*, vol. 8, no. 5, pp. 2268–2277, Sept. 2017.
[18] J. A. Suul, S. D'Arco, and G. Guidi, "Virtual synchronous machine-based control of a single-phase bi-directional battery charger for providing vehicle-to-grid services," *IEEE Trans. Ind. Appl.*, vol. 52, no. 4, pp. 3234–3244, July–Aug. 2016.
[19] J. Alipoor, Y. Miura, and T. Ise, "Power system stabilization using virtual synchronous generator with alternating moment of inertia," *IEEE J. Emerg. Sel. Topics Power Electron.*, vol. 3, no. 2, pp. 451–458, June 2015.
[20] D. Li, Q. Zhu, S. Lin, and X. Y. Bian, "A self-adaptive inertia and damping combination control of VSG to support frequency stability," *IEEE Trans. Energy Convers.*, vol. 32, no. 1, pp. 397–398, March 2017.
[21] U. Markovic, Z. Chu, P. Aristidou, and G. Hug-Glanzmann, "LQR-based adaptive virtual synchronous machine for power systems with high inverter penetration," *IEEE Trans. Sustain. Energy*, vol. 10, no. 3, pp. 1501–1512, July 2019.
[22] J. Jongudomkarn, J. Liu, and T. Ise, "Virtual synchronous generator control with reliable fault ride-through ability: a solution based on finite-set model predictive control," *IEEE J. Emerg. Sel. Topics Power Electron.*, doi: 10.1109/JESTPE.2019.2942943.
[23] S. Mishra, D. Pullaguram, S. Achary Buragappu, and D. Ramasubramanian, "Single-phase synchronverter for a grid-connected roof top photovoltaic system," *IET Renewable Power Generation*, vol. 10, no. 8, pp. 1187–1194, 2016.
[24] Y. Wang, J. Meng, X. Zhang, and L. Xu, "Control of PMSG-based wind turbines for system inertial response and power oscillation damping," *IEEE Trans. Sustain. Energy*, vol. 6, no. 2, pp. 565–574, April 2015.
[25] Y. Li, Z. Xu, and K. P. Wong, "Advanced control strategies of PMSG-based wind turbines for system inertia support," *IEEE Trans. Power Syst.*, vol. 32, no. 4, pp. 3027–3037, July 2017.
[26] S. Wang, J. Hu, and X. Yuan, "Virtual synchronous control for grid-connected DFIG-based wind turbines," *IEEE J. Emerg. Sel. Topics Power Electron.*, vol. 3, no. 4, pp. 932–944, Dec. 2015.
[27] M. A. Torres L., L. A. C. Lopes, L. A. Morán T., and J. R. Espinoza C., "Self-tuning virtual synchronous machine: a control strategy for energy storage systems to support dynamic frequency control," *IEEE Trans. Energy Convers.*, vol. 29, no. 4, pp. 833-840, Dec. 2014.
[28] J. Fang, Y. Tang, H. Li, and X. Li, "A battery/ultracapacitor hybrid energy storage system for implementing the power management of virtual synchronous generators," *IEEE Trans. Power Electron.*, vol. 33, no. 4, pp. 2820–2824, April 2018.
[29] M. Guan, W. Pan, J. Zhang, Q. Hao, J. Cheng, and X. Zheng, "Synchronous generator emulation control strategy for voltage source converter (VSC) stations," *IEEE Trans. Power Syst.*, vol. 30, no. 6, pp. 3093–3101, Nov. 2015.
[30] R. Aouini, B. Marinescu, K. Ben Kilani, and M. Elleuch, "Synchronverter-based emulation and control of HVDC transmission," *IEEE Trans. Power Syst.*, vol. 31, no. 1, pp. 278–286, Jan. 2016.
[31] S. Dong, Y. Chi, and Y. Li, "Active voltage feedback control for hybrid multiterminal HVDC system adopting improved synchronverters," *IEEE Trans. Power Del.*, vol. 31, no. 2, pp. 445–455, April 2016.
[32] Y. Cao et al., "A virtual synchronous generator control strategy for VSC-MTDC systems," *IEEE Trans. Energy Convers.*, vol. 33, no. 2, pp. 750–761, June 2018.
[33] C. Li, Y. Li, Y. Cao, H. Zhu, C. Rehtanz, and U. Häger, "Virtual synchronous generator control for damping dc-side resonance of VSC-MTDC system," *IEEE J. Emerg. Sel. Topics Power Electron.*, vol. 6, no. 3, pp. 1054–1064, Sept. 2018.
[34] D. Chen, Y. Xu, and A. Q. Huang, "Integration of DC microgrids as virtual synchronous machines into the AC grid," *IEEE Trans. Ind. Electron.*, vol. 64, no. 9, pp. 7455–7466, Sept. 2017.
[35] Q.-C. Zhong, "Virtual Synchronous Machines: A unified interface for grid integration," *IEEE Power Electron. Mag.*, vol. 3, no. 4, pp. 18–27, Dec. 2016.
[36] N. Pogaku, M. Prodanovic, and T. C. Green, "Modeling, analysis and testing of autonomous operation of an inverter-based microgrid," *IEEE Trans. Power Electron.*, vol. 22, no. 2, pp. 613–625, March 2007.
[37] M. Rasheduzzaman, J. A. Mueller, and J. W. Kimball, "An accurate small-signal model of inverter- dominated islanded microgrids using *dq* reference frame," *IEEE J. Emerg. Sel. Topics Power Electron.*, vol. 2, no. 4, pp. 1070–1080, Dec. 2014.
[38] V. Mariani, F. Vasca, J. C. Vásquez, and J. M. Guerrero, "Model order reductions for stability analysis of islanded microgrids with droop control," *IEEE Trans. Ind. Electron.*, vol. 62, no. 7, pp. 4344–4354, July 2015.
[39] K. Yu, Q. Ai, S. Wang, J. Ni, and T. Lv, "Analysis and optimization of droop controller for microgrid system based on small-signal dynamic model," *IEEE Trans. Smart Grid*, vol. 7, no. 2, pp. 695–705, March 2016.
[40] J. Liu, Y. Miura, and T. Ise, "A comparative study on damping methods of virtual synchronous generator control," in *Proc. Eur. Conf. Power Electron. Appl. (EPE – ECCE Europe)*, Genova, Italy, 2019, pp. 1–10.
[41] J. Liu, Y. Miura, and T. Ise, "Power Quality improvement of microgrids by virtual synchronous generator control," in *Proc. Elect. Power Quality Supply Rel. Conf. (PQ)*, Tallinn, Estonia, 2016, pp. 119–124.
[42] A. D. Paquette and D. M. Divan, "Virtual impedance current limiting for inverters in microgrids with synchronous generators," *IEEE Trans. Ind. Appl.*, vol. 51, no. 2, pp. 1630–1638, March–April 2015.
[43] J. Liu, Y. Miura, and T. Ise, "Cost-function-based microgrid decentralized control of unbalance and harmonics for simultaneous bus voltage compensation and current sharing," *IEEE Trans. Power Electron.*, vol. 34, no. 8, pp. 7397–7410, Aug. 2019.
[44] L. Zhang, L. Harnefors, and H. Nee, "Power-synchronization control of grid-connected voltage-source converters," *IEEE Trans. Power Syst.*, vol. 25, no. 2, pp. 809–820, May 2010.
[45] K. Ogata, *Modern Control Engineering, 5th ed*. Upper Saddle River, NJ, USA: Prentice Hall, 2010, pp. 161–179.

JIA LIU (S'15–M'17) received the B.Eng. and M.Eng. degrees from Xi'an Jiaotong University, Xi'an, China, in 2008 and 2011, respectively, the Diplôme d'Ingénieur from the University of Technology of Troyes, Troyes, France, in 2011, and the Ph.D. degree in engineering from Osaka University, Osaka, Japan, in 2016.

He was with Delta Electronics (Jiangsu), Ltd., Nanjing, China, from 2011 to 2012. Since 2016, he has been with the Division of Electrical, Electronic and Information Engineering, Graduate School of Engineering, Osaka University, where he is currently an Assistant Professor. His research interests include distributed generators, microgrids, power quality, and smart loads.

YUSHI MIURA (M'06) received the Bachelor, Master and Ph.D. degrees from Tokyo Institute of Technology in 1990, 1992 and 1995, respectively.

He was a Researcher in Japan Atomic Energy Research Institute from 1995 to 2004, and an Associate Professor at Osaka University from 2004 to 2018. He is currently a Professor at Nagaoka University of Technology. His research interests include power electronics, power engineering, energy storage system, microgrids, smart grids, and superconducting coil power supplies.

HASSAN BEVRANI (S'90–M'04–SM'08) received PhD degree in electrical engineering from Osaka University (Japan) in 2004. Currently, he is a Full Professor and the Program Leader of Smart/Micro Grids Research Center (SMGRC) at the University of Kurdistan (UOK).

Over the years, he has worked as senior research fellow and visiting professor with Osaka University, Kumamoto University (Japan), Queensland University of Technology (Australia), Kyushu Institute of Technology (Japan), Centrale Lille (France), and Technical University of Berlin (Germany).

Prof. Bevrani is the author of 6 international books, 15 book chapters, and more than 300 journal/conference papers. His current research interests include smart grid operation and control, power systems stability and optimization, Microgrid dynamics and control, and Intelligent/robust control applications in power electric industry.

TOSHIFUMI ISE (M'86) received the Bachelor of Engineering, Master of Engineering. and Doctor of Engineering degrees in electrical engineering from Osaka University, Osaka, Japan, in 1980, 1982 and 1986 respectively.

From 1986 to 1990, he was with the Nara National College of Technology, Nara, Japan. Since 1990, he had been with the Faculty of Engineering and Graduate School of Engineering, Osaka University, Osaka, Japan and was a Professor from August 2002 to March 2018. Currently, he is a Professor Emeritus of Osaka University and the President of Nara-Gakuen Incorporated Educational Institution. His research interests are in the areas of power electronics and applied superconductivity for power systems.

Prof. Ise is a fellow of the Institute of Electrical Engineers of Japan (IEEJ).